Computationally Efficient Induction Machine Model Incorporating Magnetic Saturation and Air-Gap Flux Harmonics for Offline and Real-Time Analysis

MohammadSadegh KhajueeZadeh, Arash Safavizadeh, Shadman Saqlain Rahman, Navid Amiri, and Juri Jatskevich
Department of Electrical and Computer Engineering
University of British Columbia
Vancouver, Canada
{mohammadkhajuee, arash.safavizadeh, shadman0, navida, jurij}@ece.ubc.ca

***Abstract*—For studying power systems with induction machines, especially in real-time electromagnetic transients (EMT), the machine models have to be both computationally efficient and highly accurate. In some instances, in addition to modeling the fundamental component of flux saturation, it is also necessary to consider the air-gap flux harmonics. This paper presents a computationally efficient and easy-to-implement *qd*0 model of an induction machine that considers magnetic saturation and air-gap flux distortion. The accuracy of the new model is benchmarked against the Simscape Electrical Specialized Power Systems (SPS) built-in model (which considers only the fundamental flux saturation) and the recently proposed full-order *qd*0 model (which considers both the fundamental and third harmonic). The new model is shown to have excellent agreement with the experimental results, while offering significant computational gains in offline (MATLAB/Simulink) and real-time (OPAL-RT's OP5700) simulations, making it suitable for EMT simulators.**

***Index Terms*—EMT simulation, induction machines, magnetic saturation, *qd*0 model.**

I. Introduction

The safety and reliability of power and energy systems, as well as the planning for integrating new technologies, strongly rely on the ability to study and analyze a wide range of faults and operating conditions that may arise in electrical machines. However, performing numerous realistic test cases for various operating conditions on real hardware setups is often time-consuming and costly, while also posing safety challenges. For that purpose, accurate and computationally efficient models of electrical machines, particularly induction machines, are highly desirable. Higher model fidelity provides greater insight into machine dynamics. Electromagnetic transient (EMT) simulation programs are key tools for simulating such models within electrical systems of different sizes and scales. Particularly, incorporating magnetic saturation, as one of the most significant effects that induction machines are subjected to when operating close to or slightly above their nominal voltages, is highly desirable [1].

Although several methodologies are available for modeling saturation effects in induction machines, such as finite element analysis (FEA) [2] and the winding function methods [3], their accuracy comes at the cost of being computationally expensive. For the study of multi-machine systems and/or real-time motor drives, the conventional circuit-based *qd*0 models [4] are computationally efficient and offer a trade-off between simplicity and accuracy. Accordingly, these models are often available as built-in library components in many EMT simulation programs, including nodal-analysis-based tools (e.g., PSCAD/EMTDC, EMTP), state-variable-based programs (e.g., MATLAB/ Simulink's Simscape Electrical toolbox, PLECS), and real-time simulators (e.g., RTDS's RSCAD, OPAL-RT's RT-LAB, and Typhoon HIL).

To advance fidelity of induction machine models, a wide range of *qd*0 models have been proposed, including those that consider magnetic saturation [1], [4]. In these models, the saturation is typically represented as a nonlinear relationship between the magnetizing current and main magnetizing flux [1]. However, uneven saturation of different regions of the machine, particularly the higher saturation of the stator teeth and slot areas on magnetic poles, gives rise to distortions in the air-gap flux, leading to additional harmonics. This phenomenon of air-gap flux harmonics has been recently incorporated into the general-purpose *qd*0 models [5] and advanced voltage-behind-reactance models [6], by appropriately increasing the model order and complexity.

This paper presents an easy-to-implement low-order *qd*0 model that considers the main magnetizing flux saturation fundamental and 3rd harmonic components. Compared to [5], [6], the model order is reduced by neglecting the dynamics of the 3rd harmonic components and replacing them with algebraic equations. Building upon the work in [7], the model implementation is further optimized for state-variable-based EMT simulators, such as MATLAB/Simulink, and real-time simulators, such as OPAL-RT's RT-Lab. The advantageous features of the new model are demonstrated in offline and real-time studies for single-machine and multi-machine systems. The comparisons are carried out against the conventional saturable built-in *qd*0 model in Simulink's Simscape Electrical Specialized Power Systems (SPS) model, as well as the full-order model proposed in [5]. Specifically, the low-order induction machine model presented in this paper is shown to consume less computational resources (i.e. smaller CPU time per step in offline studies, and smaller CPU utilization in OP5700 real-time simulator) compared to the full-order model [5], and even to the SPS model that includes the fundamental component of the main flux saturation only.

979-8-3315-8138-1

II. QD-Model with Magnetic Saturation and Air-Gap Flux Harmonics

This paper builds upon the previous work in [5]-[7] and uses the same notations for consistency. Within the saturation region, the magnetic flux density and magnetic field strength follow a nonlinear magnetization relationship. Hence, the magnetizing flux linkage λ_m can be written as a nonlinear function of the magnetizing current i_m, as $F\left(i_m\right)$. Due to uneven magnetic saturation, including teeth and slots over the magnetic poles, the air-gap main magnetizing flux also contains distortions, which are represented by the fundamental and 3rd harmonic, denoted by λ_{m1} and λ_{m3}, as shown in Figs. 1(a) and 1(b) [5]. These relationships are expressed as

$$\lambda_{m1} = F_1\left(i_m\right) \text{ and } \lambda_{m3} = F_3\left(i_m\right). \tag{1}$$

For a squirrel-cage induction machine, the rotor bars form a uniformly distributed winding; therefore, the rotor winding factor for low-order flux linkages is unity. Additionally, due to the short-pitch coil winding of the stator, the first-order winding factor k_{w1} and the third-order winding factor k_{w3} differ significantly as [5]. Consequently, the third-order flux linkages in the rotor and stator can be written

$$\lambda_{mr3} = \frac{1}{3}\lambda_{m3} \text{ and } \lambda_{ms3} = \frac{k_{w3}}{3k_{w1}}\lambda_{m3}. \tag{2}$$

A. *Full-Order Model*

For the purpose of modeling, the *abc* stator and first-order rotor voltages and currents are transformed into the *qd*0 synchronous reference frame with the electrical angle θ_s, as illustrated in Fig. 2(a). Meanwhile, another frame rotating three times faster, *qd*03, with an electrical angle of $3\theta_s$ is used to transform the third-order rotor voltages and currents, as shown in Fig. 2(b). Referring to the coupled-circuit phase-domain (CCPD) model in [4] and the coordinate systems shown in Fig. 2, the stator and rotor voltages of a squirrel-cage induction machine in the *qd*-synchronous frame are [5]

$$\mathbf{v}_{qds} = r_s\mathbf{i}_{qds} + p\boldsymbol{\lambda}_{qds} \pm \omega_s\boldsymbol{\lambda}_{dqs}, \tag{3}$$

$$v_{0s} = r_s i_{0s} + p\lambda_{0s}, \tag{4}$$

$$0 = r_r\mathbf{i}_{qdr} + p\boldsymbol{\lambda}_{qdr} \pm \left(\omega_s - \omega_r\right)\boldsymbol{\lambda}_{dqr}, \tag{5}$$

$$0 = r_r\mathbf{i}_{qdr3} + p\boldsymbol{\lambda}_{qdr3} \pm 3\left(\omega_s - \omega_r\right)\boldsymbol{\lambda}_{dqr3}. \tag{6}$$

Here, p, ω_s, and ω_r denote the Heaviside derivative operator *d/dt*, the synchronous reference frame angular speed, and the electrical angular speed of the rotor, respectively. Moreover, the stator and rotor currents can also be written as

$$\mathbf{i}_{qd0s} = L_{ls}^{-1}\left(\boldsymbol{\lambda}_{qd0s} - \boldsymbol{\lambda}_{mqd0}\right), \tag{7}$$

$$\mathbf{i}_{qdr} = L_{lr}^{-1}\left(\boldsymbol{\lambda}_{qdr} - \boldsymbol{\lambda}_{mqd}\right), \tag{8}$$

$$\mathbf{i}_{qdr3} = L_{lr}^{-1}\left(\boldsymbol{\lambda}_{qdr3} - \boldsymbol{\lambda}_{mqd3}\right). \tag{9}$$

The zero-sequence current of the rotor i_{0r} does not flow within the rotor cage and is therefore neglected. However, the zero-sequence voltage and current of the stator in (4) contribute to higher-order magnetizing fluxes [4].

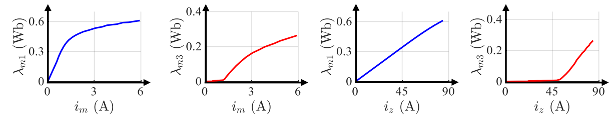

(a) (b) (c) (d)

Fig. 1. Experimentally determined magnetizing flux components [5]: (a) $\lambda_{m1} - i_m$, (b) $\lambda_{m3} - i_m$, (c) $\lambda_{m1} - i_z$, and (d) $\lambda_{m3} - i_z$.

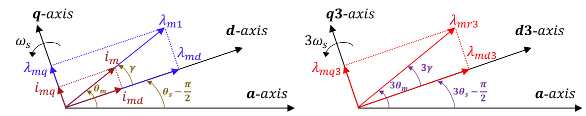

(a) (b)

Fig. 2. Phasor diagrams of the magnetizing current and flux linkages in: (a) synchronous *qd* frame, and (b) *qd*3 frame.

Substituting (7)–(9) into (3)–(6) results in the full-order *qd*0 model [5]:

$$p\boldsymbol{\lambda}_{qds} = \mathbf{v}_{qds} - r_s L_{ls}^{-1}\left(\boldsymbol{\lambda}_{qds} - \boldsymbol{\lambda}_{mqd}\right) \mp \omega_s\boldsymbol{\lambda}_{dqs}, \tag{10}$$

$$p\lambda_{0s} = v_{0s} - r_s L_{ls}^{-1}\left(\lambda_{0s} - \lambda_{m0}\right), \tag{11}$$

$$p\boldsymbol{\lambda}_{qdr} = -r_r L_{lr}^{-1}\left(\boldsymbol{\lambda}_{qdr} - \boldsymbol{\lambda}_{mqd}\right) \mp \left(\omega_s - \omega_r\right)\boldsymbol{\lambda}_{dqr}, \tag{12}$$

$$p\boldsymbol{\lambda}_{qdr3} = -r_r L_{lr}^{-1}\left(\boldsymbol{\lambda}_{qdr3} - \boldsymbol{\lambda}_{mqd3}\right) \mp 3\left(\omega_s - \omega_r\right)\boldsymbol{\lambda}_{dqr3}. \tag{13}$$

According to Fig. 2, λ_{md}, λ_{mq}, λ_{md3}, and λ_{mq3}, corresponding to the first- and third-order magnetizing fluxes along the *d*- and *q*-axes, can be written as

$$\lambda_{mq} = \lambda_{m1}\sin\left(\gamma\right) \text{ and } \lambda_{md} = \lambda_{m1}\cos\left(\gamma\right), \tag{14}$$

$$\lambda_{mq3} = \lambda_{mr3}\sin\left(3\gamma\right) \text{ and } \lambda_{md3} = \lambda_{mr3}\cos\left(3\gamma\right). \tag{15}$$

Here, the angle γ displayed in Fig. 2(a) is written as $\gamma = \theta_m - \theta_s + \pi/2$, and defines the angle between the magnetizing current vector and the *d*-axis (i.e., the angle between λ_{m1} and λ_{md}). Moreover, the angle between λ_{mr3} and λ_{md3} is three times larger, that is, 3γ as shown in Fig. 2(b). In (11), λ_{m0} oscillates at a frequency three times higher than the stator electrical frequency. The angle between the third-order rotor magnetizing flux and the *a*-axis is $3\theta_m$, as shown in Fig. 2(b), where θ_m is the angle between the magnetizing current (or flux linkage) and the *a*-axis. Based on this model, the oscillatory flux component that will appear in the zero-sequence stator circuit λ_{m0} can be written as

$$\lambda_{m0} = \lambda_{ms3}\sin\left(3\theta_s + 3\gamma - 3\pi/2\right). \tag{16}$$

Following the inclusion of third-order rotor fluxes and currents into the *qd*0 model, the final electromagnetic torque T_e is expressed as

$$T_e = \left(\frac{3P}{4}\right)\left[\left(\lambda_{md}i_{qs} - \lambda_{mq}i_{ds}\right) + 3\left(\lambda_{mq3}i_{dr3} - \lambda_{md3}i_{qr3}\right)\right], \tag{17}$$

where P denotes the number of poles.

However, direct use of (1) for implementing the model results in algebraic loops, making the model formulation implicit, computationally expensive, and not suitable for real-time execution without numerical relaxation (a time step

979-8-3315-8138-1

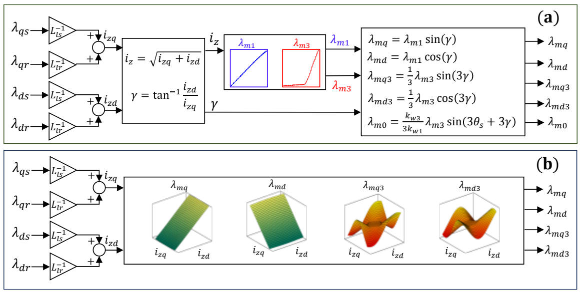

Fig. 3. Explicit flux correction methods: (a) with two 1-D LUTs and algebraic calculations, and (b) with four two-input (i_{zdq}) one-output 2-D LUTs for the first- and third-order magnetizing fluxes of the *d*- and *q*-axes.

delay). Alternatively, [1] defines an explicit-flux-correction method in which intermediate variables, currents $i_{zq} = L_{ls}^{-1}\lambda_{qs} + L_{lr}^{-1}\lambda_{qr}$ and $i_{zq} = L_{ls}^{-1}\lambda_{qs} + L_{lr}^{-1}\lambda_{qr}$ are introduced as functions of the state variables (fluxes). Subsequently, the vector $i_z = \sqrt{i_{zq}^2 + i_{zd}^2}$ is also aligned with the magnetizing current i_m. Thereafter, it becomes possible to express the magnetizing fluxes λ_{m1} and λ_{m3} in terms of the magnitude of the intermediate variable (current) i_z instead of magnetizing current i_m, as shown in Figs. 1(c) and (d). Hence, the fundamental and third-order magnetizing fluxes of (1) are expressed as [5]

$$\lambda_{m1} = G_{z1}(i_z) \text{ and } \lambda_{m3} = G_{z3}(i_z). \tag{18}$$

Based on (18), with the input i_z and outputs λ_{m1} and λ_{m3}, the calculation of fluxes can be implemented explicitly according to Fig. 3(a) using two one-dimensional (1-D) look-up tables (LUTs). This explicit implementation also requires sequentially performing algebraic calculations, referring to (14) and (15) to obtain λ_{md}, λ_{mq}, λ_{md3}, and λ_{mq3} from λ_{m1} and λ_{m3}. Alternatively, to reduce the number of evaluations of nonlinear trigonometric functions, an equivalent implementation may be realized using two-input one-output 2-D LUTs, as shown in Fig. 3(b), which offers straightforward calculation of λ_{md}, λ_{mq}, λ_{md3}, and λ_{mq3} from input pairs of i_{zd} and i_{zq}. Meanwhile, the calculation of λ_{m0} is unchanged from that in Fig. 3(a), as it is an oscillatory term.

B. *Low-Order Model*

Carrying extra state equations (13) is computationally expensive. Assuming the third-order rotor flux linkages λ_{qr3} and λ_{dr3} are significantly smaller than fundamental component linkages (see Fig. 1), their transients can be neglected. Thus, setting the derivatives $p\lambda_{qr3}$ and $p\lambda_{dr3}$ to zero [7], resulting in algebraic constraints as

$$0 = -r_r L_{lr}^{-1}\left(\boldsymbol{\lambda}_{qdr3} - \boldsymbol{\lambda}_{mqd3}\right) \mp 3(\omega_s - \omega_r)\boldsymbol{\lambda}_{dqr3}, \tag{19}$$

which has an algebraic solution for λ_{qr3} and λ_{dr3} as

$$\lambda_{qr3} = \frac{(r_r/L_{lr})^2 \lambda_{mq3} + 3(r_r/L_{lr})(\omega_s - \omega_r)\lambda_{md3}}{(r_r/L_{lr})^2 + 9(\omega_s - \omega_r)^2}, \tag{20}$$

$$\lambda_{dr3} = \frac{(r_r/L_{lr})^2 \lambda_{md3} - 3(r_r/L_{lr})(\omega_s - \omega_r)\lambda_{mq3}}{(r_r/L_{lr})^2 + 9(\omega_s - \omega_r)^2}. \tag{21}$$

This approximation reduces the model order from seven to five and improves computational efficiency. Fig. 4 displays a block diagram of the proposed model implementation.

III. Model Performance

To evaluate the proposed model and benchmark it against alternative models, a Y-connected, grounded-neutral induction motor is considered supplied from an AC grid. The connection of the neutral point enables the monitoring of the zero-sequence current, and it may sometimes be used for protection. In the considered studies, full-order [5], proposed low-order, and SPS models were first analyzed offline in MATLAB/Simulink. Moreover, steady-state measurements from a 230 V, 0.25 hp squirrel-cage induction machine, as shown in Fig. 5, are obtained to verify the proposed model experimentally. The data corresponding to the induction machine shown in Fig. 5 are given in the Appendix.

A. *Time-Domain Verification*

Fig. 6 shows the phase voltages and currents under 1.0 pu and 1.4 pu input voltages, respectively, for the SPS built-in model and the proposed low-order model, considering only the fundamental flux component saturation. As seen in Fig. 6, both models exhibit similar behaviour.

Fig. 7 displays the results of the SPS built-in model (considering only the fundamental component flux saturation); and the full-order model [5] and the proposed low-order model that includes the fundamental and 3rd harmonic saturation, under 1.0 pu and 1.4 pu input voltages, respectively. As seen in Fig. 7(b), under a 1.0 pu grid voltage, the emergence of air-gap flux distortion propagates to the phase currents of the induction machine, and becomes even more pronounced with an increased input voltage to 1.4 pu. In this case, both the full-order and low-order models offer high fidelity in capturing the third-order distortions in current. At the same time, the SPS model is unable to predict this effect as it only accounts for the fundamental component of the main magnetizing flux.

To further verify the proposed methodology, the experimental hardware measurements under steady-state conditions with 1.0 pu and 1.4 pu input voltages are also included in Fig. 8. These results are also compared to the simulated waveforms produced by the full-order [5] and proposed low-order models when supplied with the recorded grid voltages (reproduced in the simulation for input consistency). As can be seen from the currents in Fig. 8, the models that include the fundamental and 3rd harmonic flux saturation are in excellent agreement with the measurements.

B. *Computational Efficiency*

To benchmark the proposed low-order model against the full-order model [5] and the built-in SPS model, all models

979-8-3315-8138-1

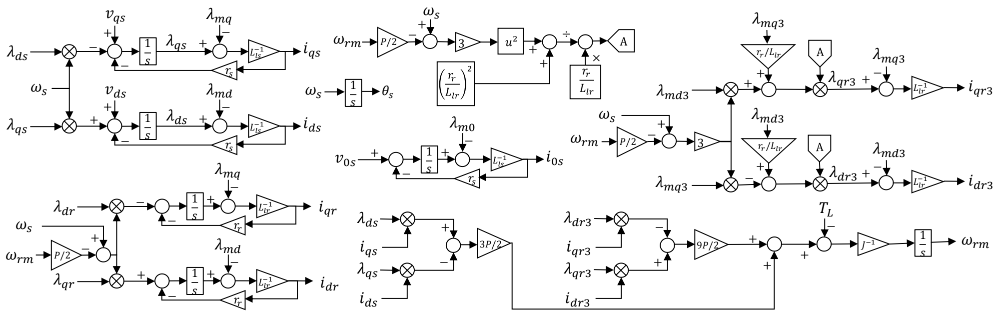

Fig. 4. Block diagram of the proposed low-order model implementation in MATLAB/Simulink.

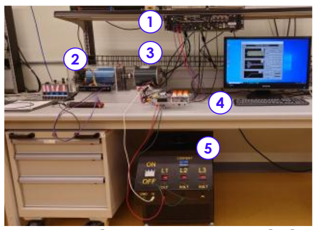

Fig. 5. Test bench for experimental measurements, including (1) measurement box, (2) DC load machine, (3) test induction machine, (4) data acquisition and recording system, and (5) three-phase power supply [5].

were analyzed using the fixed-step *ode*3 solver. The fixed step sizes were set to 5 µs, 50 µs, and 500 µs to identify which models maintain validity at larger step sizes. This enabled the measurement of runtime and CPU utilization for each model in both offline and real-time analyses. In addition to analyzing each model individually, multi-machine configurations were examined to assess scalability, thereby supporting the objective of proposing a low-order model suitable for large-scale systems. All offline studies were conducted on a PC with an Intel Core i7-14700 CPU at 2.10 GHz. For real-time simulations, both single-machine and multi-machine configurations were run on an OPAL-RT OP5700 simulator with an Intel® Xeon® E5 CPU (2 cores, 3.2 GHz, 20 MB cache, 8 GB memory), as shown in Fig. 9. RT-LAB is the software that converts MATLAB/Simulink models into real-time executable code and distributes the processing tasks across the available CPU cores for execution on the OPAL-RT hardware. In Table I, the CPU times from offline MATLAB/Simulink studies and the CPU utilization percentages in real-time on the OPAL-RT are shown for all models under different machine-number configurations, with time steps ranging from 5 µs to 500 µs. Moreover, Table II shows the maximum number of machine models that can be run in real time on the OPAL-RT for each model at time steps of 5 µs and 50 µs, without encountering overruns/overflow.

1) Offline Computer Studies

According to Table I, the proposed low-order model in single-machine studies with a 5-µs time step is approximately 23% and 30% faster than the full-order and SPS models, respectively. Moreover, for large-scale multi-machine studies, the proposed model achieves 33% and 63% runtime reduction for a 4-machine system at 5 µs. This benefit becomes more significant for a 60-machine system, for which the proposed model is approximately 1.6 and 2.2 times more efficient computationally than the full-order and SPS models, respectively.

2) Real-Time Simulator Studies

For single-machine real-time simulations at a 5-µs time step, the proposed low-order model achieves 22% and 26% lower CPU utilization compared to the full-order and SPS models, respectively. For the multi-machine configurations, the proposed low-order model enables real-time simulation of four induction machines, yielding a CPU utilization of 53.85% at a 5-µs time step. In contrast, the maximum feasible number of machines for the full-order and SPS models under the same conditions is three and two, with CPU utilization of 59.64% and 43.64%, respectively (see Table II). Moreover, the proposed model allows large-scale real-time studies, providing the capability to simulate 65 machines at a 50-µs time step with a CPU utilization of 92.25%. This number is smaller for the full-order and SPS models, which can simulate at most 50 and 45 machines, with CPU utilization of 93.65% and 95.2%, respectively. Thus, at a 50-µs time step, the proposed model enables the simulation of approximately 30% and 44% more machines than the full-order and SPS models, respectively. A similar advantage holds for small time steps, such as 5 µs, where the proposed model enables the study of approximately 1.3 to 2 times more machines, respectively, in real-time. Note that all the CPU utilization and maximum feasible machine numbers in Tables I and II did not result in any overruns or overflow in the real-time simulator. However, increasing the number of machines above the specified figures in Tables I and II resulted in overruns/overflow calculations leading to a loss of real-time synchronization at some time steps.

IV. Conclusion

Incorporating the air-gap flux distortions into the induction machine saturation increases the model fidelity and produces results that are closer to the experimental measurements of the machine under saturation. Most widely available *qd*0 models, such as the SPS built-in model, only consider fundamental component flux saturation and therefore are unable to reproduce accurate results of current distortion due to the saturation phenomenon. The alternative models that consider the 3rd harmonic flux saturation are generally more complicated to implement and costly to simulate. This paper presented an easy-to-implement and computationally efficient induction machine model that captures the saturation of both the fundamental and 3rd harmonics of the magnetizing flux. According to the presented offline and real-time simulations, the proposed low-order model offers significant computational advantages for single-machine and multi-machine studies, making it a potentially suitable choice for large-scale EMT studies involving numerous induction machines.

979-8-3315-8138-1

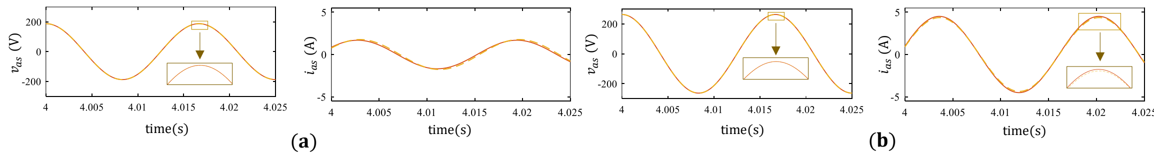

Fig. 6. Steady-state stator voltages and currents for the low-order *qd* model (yellow dashed line) and the SPS model (red solid line) at grid voltages of (a) 1.0 pu and (b) 1.4 pu, without integration of third-order air-gap flux.

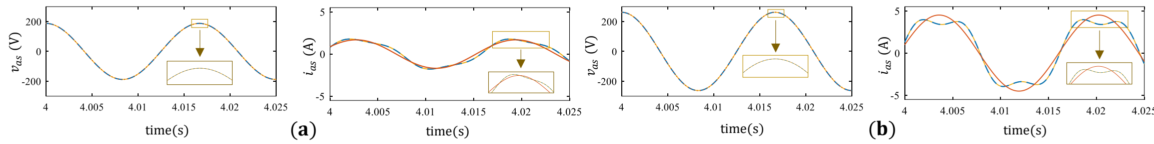

Fig. 7. Steady-state stator voltages and currents for the full-order model (blue dashed line), low-order model (yellow dashed line), and SPS model (red solid line) at grid RMS voltages of (a) 1.0 pu and (b) 1.4 pu, with integration of third-order air-gap flux

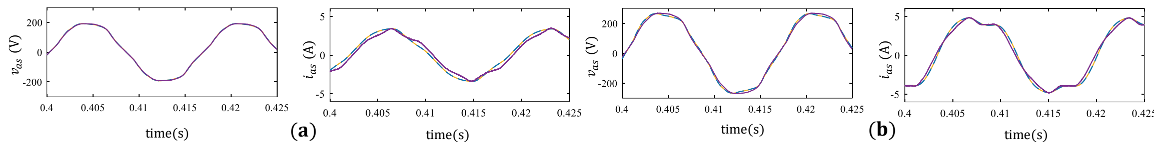

Fig. 8. Steady-state stator voltages and currents for the full-order model (blue dashed line), low-order model (yellow dashed line), and hardware measurements (purple solid line) at grid RMS voltages of (a) 1.0 pu and (b) 1.4 pu. The experimentally recorded grid voltages were saved and injected into the simulations.

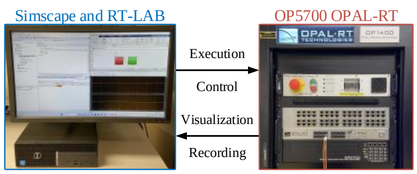

Fig. 9. Model execution on the OPAL-RT OP5700 real-time simulator using Simulink/RT-LAB software.

TABLE I. CPU TIMES AND CPU OCCUPANCY PERCENTAGES OF THE SUBJECT MODELS FOR OFFLINE AND REAL-TIME ANALYSES

Offline CPU Time (s)				
Models	Numbers	Δt = 5 μs	Δt = 50 μs	Δt = 500 μs
Low-order	1	19.32	1.61	0.20
Full-order		23.80	2.23	0.25
SPS		25.01	2.53	N/V
Low-order	4	64.06	5.80	0.64
Full-order		85.33	8.41	0.93
SPS		104.2	10.75	N/V
Low-order	60	1863.45	181.84	17.78
Full-order		2901.34	296.88	28.31
SPS		4065.37	417.73	N/V
Real-Time CPU Occupancy (%)				
Low-order	1	21.79	2.49	0.26
Full-order		26.58	2.90	0.30
SPS		27.53	3.01	N/V*
Low-order	4	53.85	8.32	0.84
Full-order		O/L**	10.92	1.12
SPS		O/L	11.21	N/V
Low-order	60	O/L	76.27	10.75
Full-order		O/L	O/L	11.24
SPS		O/L	O/L	N/V

***N/V** denotes that the SPS model results are not valid at a 500-μs time step.
****O/L** denotes an overload condition of the CPU in the real-time simulator.

APPENDIX

Induction Motor Parameters:

230V, 0.25hp, 4 poles, r_s = 6.5 Ω, r_r = 6.6 Ω, L_m = 350 mH, L_{ls} = 26 mH, L_{lr} = 11.1 mH, k_{w1} = 0.9, k_{w3} = 0.33.

TABLE II. MAXIMUM FEASIBLE MACHINE NUMBERS AND CPU OCCUPANCIES IN REAL-TIME MULTI-MACHINE CONFIGURATIONS

Models	Max Feasible Machine Numbers	CPU Occupancy (%)
Δt = 5 μs		
Low-order	4	53.85
Full-order	3	59.64
SPS	2	43.64
Δt = 50 μs		
Low-order	65	92.25
Full-order	50	93.65
SPS	45	95.2

REFERENCES

[1] F. Therrien, L. Wang, J. Jatskevich, and O. Wasynczuk, "Efficient explicit representation of AC machines main flux saturation in state-variable-based transient simulation packages," *IEEE Trans. Energy Conv.*, vol. 28, no. 2, pp. 380–393, Jun. 2013.

[2] L. A. Pereira, C. C. Scharlau, L. F. A. Pereira, and S. Haffner, "Influence of saturation on the air-gap induction waveform of five-phase induction machines," *IEEE Trans. Energy Conv.*, vol. 27, no. 1, pp. 29–41, Mar. 2012.

[3] S. Nandi, "A detailed model of induction machines with saturation extendable for fault analysis," *IEEE Trans. Ind. Appl.*, vol. 40, no. 5, pp. 1302–1309, Sep. 2004.

[4] X. Tu, L.-A. Dessaint, R. Champagne, and K. Al-Haddad, "Transient modeling of squirrel-cage induction machine considering air-gap flux saturation harmonics," *IEEE Trans. Ind. Electron.*, vol. 55, no. 7, pp. 2798–2809, Jul. 2008.

[5] N. Amiri, S. Ebrahimi, and J. Jatskevich, "Induction machine modeling considering magnetizing flux saturation with air-gap harmonics," *IEEE Trans. Energy Conv.*, vol. 36, no. 4, pp. 3376–3386, Dec. 2021.

[6] N. Amiri, S. Ebrahimi, and J. Jatskevich, "Saturable Voltage-Behind-Reactance Models of Induction Machines Including Air-Gap Flux Harmonics," *IEEE Trans. Energy Conv.*, Vol. 38, Iss. 3, pp. 2022 – 2033, Sep. 2023.

[7] M. KhajueeZadeh *et al.*, "Low-Order Induction Machine Model with Saturation and Air-Gap Flux Harmonics," *2025 The 10th International Conference on Power and Renewable Energy (ICPRE)*, Shanghai, China, Sep. 2025, pp. 1-6.

979-8-3315-8138-1